Available online at www.sciencedirect.com
SCIENCE DIRECT®
Journal of Sound and Vibration 284 (2005) 685–703
JOURNAL OF SOUND AND VIBRATION
www.elsevier.com/locate/jsvi

AI vibration control of high-speed rotor systems using electrorheological fluid

Seungchul Lim[a,*], Sang-Min Park[a], Kab-Il Kim[b]

[a]*Department of Mechanical Engineering, San 38-2, Nam-Dong, Yongin, 449-728, Myongji University, Yongin, South Korea*
[b]*Department of Electrical Engineering, San 38-2, Nam-Dong, Yongin, 449-728, Myongji University, Yongin, South Korea*

Received 13 December 2002; received in revised form 13 January 2004; accepted 5 July 2004
Available online 21 November 2004

Abstract

This paper is concerned with the design and application of an electrorheological (ER) fluid damper to semiactive vibration control of rotor systems. In particular, the system under the present study is constructed structurally flexible in order to explore the behavior of a high-speed spindle system traversing multiple critical speeds within motor capacity. To seek a way of suppressing the rotor vibration, dynamic models for the proposed ER damper and its associated amplifier are derived. Subsequently, they are assembled with the other relevant spindle components by means of the finite element method, enabling predictions as to free and forced vibration characteristics of the entire rotor system. Next, an artificial intelligent (AI) feedback controller is synthesized based on the system model, taking into account the stiffening effect of the point damper in flexible rotor applications. Finally, computational and experimental results are presented regarding model validation and control performances. In practice, such an AI control scheme proves effective and robust whether the spin rate is either below or above the critical speeds.

1. Introduction

Lately, for most rotating machinery including information storage devices, machine tools, and gas turbines, further performance enhancement is in demand in terms of speed and accuracy.

*Corresponding author. Tel.: +82 31 330 6428; fax: +82 31 321 4959.
E-mail address: slim@mju.ac.kr (S. Lim).

0022-460X/$ - see front matter © 2004 Elsevier Ltd. All rights reserved.
doi:10.1016/j.jsv.2004.07.014

Meanwhile, their masses tend to decrease to conserve resources so that the machines are likely to face severer, self-excited vibrations than ever caused by various vibration sources such as mass unbalance, bearing defect, and shaft misalignment. These vibrations are in turn responsible for not only performance degradations but also excessive acoustic noises and fatigue-related damages.

From that perspective, vibration suppression is a matter of great significance to rotating spindle systems. To this end, one can think of three kinds of approaches: passive, active, and semiactive controls [1–3]. Of those, the semiactive method, favorable in view of both stability and performance, is to be explored here utilizing an intelligent material, namely electrorheological (ER) fluid. Consisting of dielectric particles and non-conducting oil as the medium, the fluid can instantly and reversibly transform its phase from liquid to solid upon exposure to an electric field. It is due to the polarization phenomenon in which the particles form a network of chains across electrodes.

In fact, such smart property motivates the ER fluid diversely used for innovations of flow control valves, clutches, dampers, and so forth [4–6]. However, it has been rarely exploited for rotating structures only with a few applications, where making it less successful relatively massive and complex squirrel-cage-type dampers were employed in conjunction with a rather primitive control method [3,7], or the fluid was used as the lubricant itself for controllable journal bearings [8].

In this work, to improve the performance of rotor-bearing systems, a compact ER damper is designed and constructed anew, which is handily usable and applied to a flexible spindle system exhibiting high-speed characteristics. Moreover, in order to predict and analyze system performances, mathematical models for the damper and its associated amplifier are derived and subsequently assembled with finite element models for the other relevant spindle components [9] to obtain the system equations of motion. Next, taking into account the stiffening effect of the point damper in flexible rotor applications, which has been only vaguely uncovered so far [3,7], an AI-type [10] feedback controller is synthesized. Finally, the free and forced vibration characteristics are computed and compared with experimental results to verify the model and the predicted control performances.

For experiments, a test rig is built of a slender shaft supported by dual ball bearings, and a thin circular disk at the mid-span as illustrated in Fig. 1. In order to explore the system behaviors in supercritical speed ranges as well, the driving motor of a limited capacity is raised in speed by a simple gear train, and a flexible coupling is installed to smoothly transmit the rotational power isolating motor vibration. In addition, a pair of gap sensors is orthogonally placed near the shaft to detect whirl magnitudes and orbits.

2. Dynamic model for the ER damper

The designed ER damper has the shape of an axisymmetric, thin circular cylinder with its cross-sectional view as in Fig. 2. Once its housing is externally fixed, the disk inside the damper does not rotate along with the spindle due to the presence of a ball bearing on the inner rim and the sufficient torsional stiffness the sealing rubber pad has. Instead, the disk is to translate in the electric field developed in between the housing and itself. During the motion, friction takes place

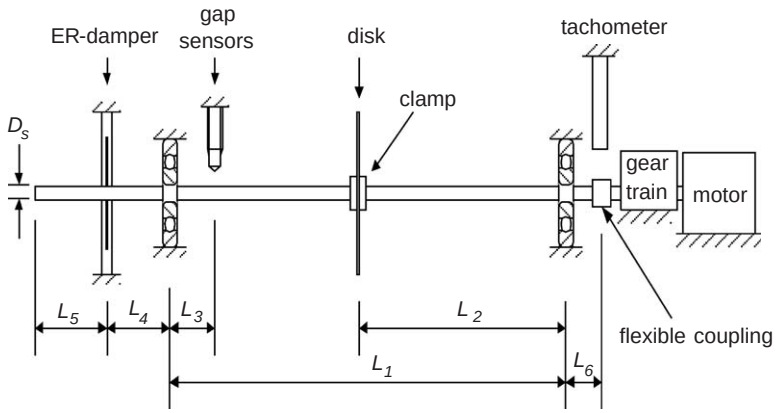

Fig. 1. Schematic diagram of the test rig.

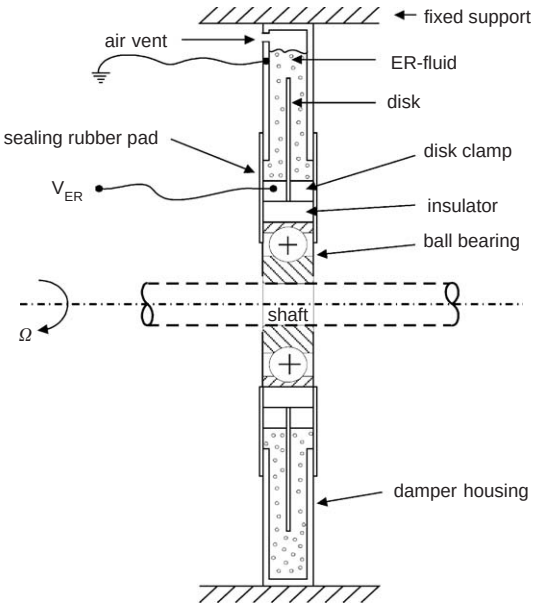

Fig. 2. Designed ER damper.

in the fashion of continuous breakage of the reforming particle chains within the ER fluid dissipating kinetic energy. Such a feature qualifies the device as a damper.

Since any long-term use of the damper is to raise the internal temperature to build up considerable air pressure pushing down the fluid, either the fluid may leak or the dielectric particles may sediment, resulting in a short circuit between the electrodes. To prevent those situations, an air vent is also pierced at the top area.

Ideally, the designed ER damper can be modeled as a spring–mass–damper system. In Fig. 3, m_{ER}, k_{ER}, and F_{fY} signify the entire movable mass including the disk, the stiffness of the sealing

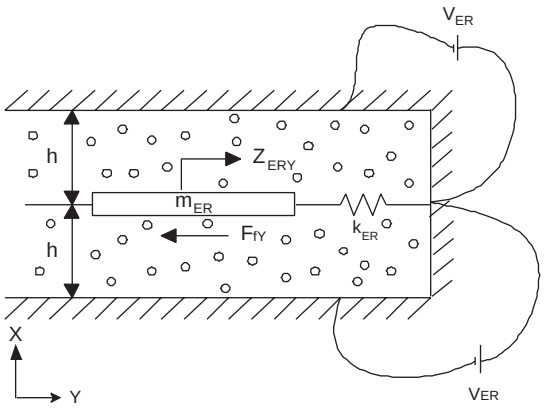

Fig. 3. Idealized ER damper model.

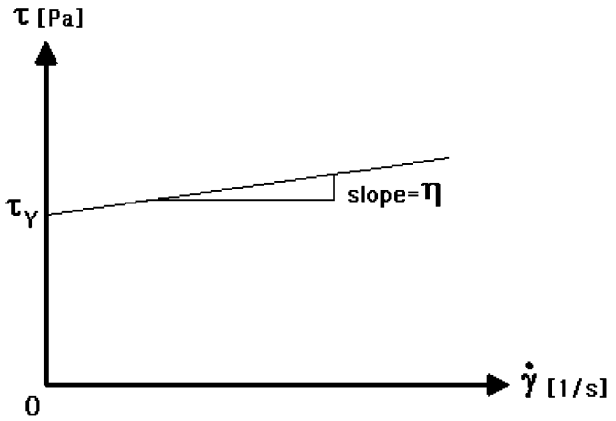

Fig. 4. Bingham fluid model.

pad, and the friction force exerted on the mass by the ER fluid, respectively. Applying Newton's law, its equation of motion can be readily obtained as below:

$$m_{\mathrm{ER}}\ddot{Z}_{\mathrm{ER}\,Y} + k_{\mathrm{ER}}Z_{\mathrm{ER}\,Y} = -F_{fY}, \tag{1}$$

where $Z_{\mathrm{ER}\,Y}$ denotes the displacement of the translating disk along the Y-axis in the fixed inertial coordinate frame $\{XYZ\}$ or briefly $\{0\}$.

The friction force can be detailed when the ER fluid is assumed to behave according to the non-Newtonian, Bingham fluid characteristics [11] portrayed in Fig. 4:

$$F_{fY} = (\tau_Y + \eta\dot{\gamma})n2\pi(R_o^2 - R_i^2), \tag{2}$$

where $\tau_Y = \alpha E^{\beta}$ denotes the yielding shear stress over which the fluid starts flowing and α and β are fluid constants; $E = V_{\mathrm{ER}}/h$ the intensity of the imposed electric field with V_{ER} and h, respectively, the input voltage and the electrode gap; η the viscosity; $\dot{\gamma}$ the shear rate; n the total

number of disks inside the damper; R_o and R_i, respectively, the inner and outer radii of the disk. Of those, the shear rate is $\partial \dot{Z}_{\mathrm{ER}Y}/\partial X$ by definition, but it can be approximated as $\dot{Z}_{\mathrm{ER}Y}/h$, since the gap between the electrodes is narrow enough.

Combining all the foregoing relationships, Eq. (1) can be rearranged as

$$m_{\mathrm{ER}}\ddot{Z}_{\mathrm{ER}Y} + c_{\mathrm{ER}}\dot{Z}_{\mathrm{ER}Y} + k_{\mathrm{ER}}Z_{\mathrm{ER}Y} = -F_{\mathrm{ER}Y}, \tag{3}$$

where the viscous friction coefficient and the Coulomb friction force amount to $c_{\mathrm{ER}} = 2\pi n(R_o^2 - R_i^2)\eta/h$ and $F_{\mathrm{ER}Y} = 2\pi n(R_o^2 - R_i^2)\alpha(V_{\mathrm{ER}}/h)^\beta \operatorname{sgn}(\dot{Z}_{\mathrm{ER}Y})$, respectively. Hence, the Coulomb friction is expected to prevail over the viscous friction when the input voltage exceeds a certain limit with the shear rate moderate.

Hereto only a single degree of freedom (dof) has been considered. In fact, the same reasoning can be extended to the motion along the perpendicular direction, $Z_{\mathrm{ER}Z}$, as well if the whole system including the damper is isotropic. So defining $\mathrm{j} = \sqrt{-1}$ and $Z_{\mathrm{ER}} = Z_{\mathrm{ER}Y} + \mathrm{j}Z_{\mathrm{ER}Z}$, the pursued 2-dof equation of motion can be expressed as below, reflecting that the friction force acts along the direction opposite to the whirl motion:

$$m_{\mathrm{ER}}\ddot{Z}_{\mathrm{ER}} + c_{\mathrm{ER}}\dot{Z}_{\mathrm{ER}} + k_{\mathrm{ER}}Z_{\mathrm{ER}} = -F_{\mathrm{ER}}, \tag{4}$$

where F_{ER} equals $F_{\mathrm{ER}Y}$ with $\dot{Z}_{\mathrm{ER}Y}$ replaced by $\dot{Z}_{\mathrm{ER}}$ in its expression above, and the signum function for complex numbers is defined such that $\operatorname{sgn}(\cdot) = (\cdot)/|\cdot|$.

Eq. (4) can be rewritten with respect to another coordinate frame $\{1\}$ that rotates with the spindle at the same speed, Ω, by a coordinate transformation of $Z_{\mathrm{ER}} = \mathrm{e}^{\mathrm{j}\Omega t} z_{\mathrm{ER}}$.

$$m_{\mathrm{ER}}\ddot{z}_{\mathrm{ER}} + (c_{\mathrm{ER}} + 2\mathrm{j}\Omega m_{\mathrm{ER}})\dot{z}_{\mathrm{ER}} + (k_{\mathrm{ER}} + \mathrm{j}\Omega c_{\mathrm{ER}} - \Omega^2 m_{\mathrm{ER}})z_{\mathrm{ER}} = -f_{\mathrm{ER}}, \tag{5a}$$

in which z_{ER} corresponds to the displacement of the damper disk observed in the frame $\{1\}$, and the complex Coulomb friction force turns out to be

$$f_{\mathrm{ER}} = 2\pi n(R_o^2 - R_i^2)\alpha(V_{\mathrm{ER}}/h)^\beta \operatorname{sgn}(\mathrm{j}\Omega z_{\mathrm{ER}} + \dot{z}_{\mathrm{ER}}). \tag{5b}$$

Indeed, Eq. (5) is valid only when the vibration speed at the damper location is other than zero. If the speed is zero or extremely small from the viewpoint of numerical computations, the Coulomb friction force will differ from Eq. (5b), balancing all the external plus spring forces exerted on the disk so that the body continues to be stationary. In the upcoming section, the friction force in such a case, also known as sticktion, is to be quantified in more detail.

In general, contemporary ER fluids function only under high-intensity electrical field, which require high-voltage amplifiers as well as narrow electrode gaps. Such amplifiers can be modeled as a first-order linear system acknowledging the inevitable time delay while neglecting the nonlinearity between the input and the output voltages:

$$\tau_A \dot{V}_{\mathrm{ER}} + V_{\mathrm{ER}} = K_A V_o, \tag{6}$$

in which τ_A and K_A mean the time constant and the steady-state voltage gain of the amplifier, respectively.

3. Equations of motion for the entire rotor system

For the entire rotor system on the left of the gear train in Fig. 1, a dynamic model can be derived with respect to the rotating frame {1} by properly assembling the damper equation (5) with the relevant element equations available in Ref. [9]. All the other spindle components such as the main shaft, the rotating disk, and the bearing are modeled as elastic, including the centrifugal effect on the disk. Besides, the employed flexible coupling is approximated as a rigid disk supported by a bearing at each end face in the form of a lumped model to reflect its mass and supportiveness. Undoubtedly, the element equation for the rigid disk is easy to derive from the flexible one simply by eliminating the out-of-plane displacement dofs.

Below are the finite element equations of motion describing how the rotor responds to input forces:

$$M\ddot{\mathbf{z}} + (C + \mathrm{j}\Omega G)\dot{\mathbf{z}} + (K_0 + \mathrm{j}\Omega K_1 + \Omega^2 K_2)\mathbf{z} = \mathbf{Q}_{\mathrm{EX}} + \mathbf{Q}_{\mathrm{ER}}, \tag{7a}$$

where $\mathbf{z}$ represents the vector of complex displacements at all nodes. All the involved coefficient matrices are symmetric: M, C, and G denote the overall mass, nonrotating damping, and gyroscopic matrices, respectively, whereas K_0, K_1, and K_2 the constant parts of the overall stiffness matrix arranged as a second-order polynomial in Ω. Also, $\mathbf{Q}_{\mathrm{EX}}$ means the excitation force vector, and $\mathbf{Q}_{\mathrm{ER}}$ the Coulomb friction force vector composed of all zero entries, except f_{ER} for the present system configuration.

Applying the aforementioned coordinate transformation to the last equation, one can have its counterpart relative to {0}:

$$M\ddot{\mathbf{Z}} + \{C + \mathrm{j}\Omega(G - 2M)\}\dot{\mathbf{Z}} + \{K_0 + \mathrm{j}\Omega(K_1 - C) + \Omega^2(K_2 - M + G)\}\mathbf{Z} = \mathrm{e}^{\mathrm{j}\Omega t}(\mathbf{Q}_{\mathrm{EX}} + \mathbf{Q}_{\mathrm{ER}}), \tag{7b}$$

whose terms now represent physically meaningful forces. Hence, referring once again to the magnitude of Coulomb friction force in the case of sticktion,

$$\begin{aligned}\mathbf{Q}_{\mathrm{ER}} &= [0 \quad 0..f_{\mathrm{ER}}..0]^{\mathrm{T}} \\ &= \mathbf{Q}_{\mathrm{EX}} - \mathrm{j}\Omega(G - 2M)(\mathrm{j}\Omega\mathbf{z} + \dot{\mathbf{z}}) - \{K_0 + \Omega^2(K_2 - M + G)\}\mathbf{z} \quad \text{for } |\dot{Z}_{\mathrm{ER}}| = 0.\end{aligned} \tag{8}$$

The derivation process of Eq. (8) involves the coordinate transformation from $\mathbf{Z}$ to $\mathbf{z}$, and the use of identity between K_1 and C, both of which consist of viscous damping coefficients related to the ball bearings and the ER damper.

Now combining the state space form of Eq. (7) with Eq. (6), the model for the entire system with actuator dynamics can be formulated:

$$\dot{\mathbf{y}} = \mathbf{f}(\mathbf{y}, V_o), \tag{9}$$

where $\mathbf{f}$ is the nonlinear function vector, and $\mathbf{y} = [\mathbf{z}^{\mathrm{T}}\ \dot{\mathbf{z}}^{\mathrm{T}}\ V_{\mathrm{ER}}]^{\mathrm{T}}$ is the state vector. Based on the above system equation, controller synthesis is possible, as well as various free and forced vibration analyses regarding the system with the help of already established methods [12,13].

4. AI feedback controller

According to the previous researches [3,7] and the current experimental observations to be presented shortly, it can be inferred that the ER damper under a constant voltage will exhibit both positive and negative effects in terms of whirl suppression as the rotor traverses resonance speeds. Hence, it is desired to properly adjust the voltage magnitude depending upon the spin speed.

To this end, several candidates may be conceived [14]. Of them, a bang–bang-type control could be attempted as in Refs. [3,7] by switching the voltage to either maximum or minimum (usually, 0 V) range after range, provided the critical speeds are identified a priori. However, such an approach cannot adapt to numerous or even a specific system on its own because system parameters may vary affecting the critical speeds. On the contrary, the well-known PID control might be suggested to detect and regulate state variables like the whirl radius, $r = \sqrt{Y^2 + Z^2}$, to zero without regard to the spin speed. Still, the scheme will experience the adverse effect somewhere above each critical speed because the constituent, proportional control action causes the stiffening effect [2].

Hence, an AI feedback controller is here proposed usable at any constant speed with no negative effects. It has a logic that states

$$\text{If } \partial r_{\text{ave}}/\partial V_{\text{ER}} > 0, \text{ then } u = 0. \quad \text{Else, } u = V_{\text{ER max}}/K_A. \tag{10}$$

In other words, the change of whirl radius vs. the applied voltage increment is to be monitored while the spin speed is nearly constant. Depending on its sign, either the lowest, zero voltage or the highest, $V_{\text{ER max}}/K_A$ is to be output and maintained until the spin speed alters. In so doing, it is advisable to evaluate the derivative, practically equal to $\Delta r_{\text{ave}}/\Delta V_{\text{ER}}$, based on the whirl radius averaged among the ones that are reliably available after a certain transient time t_d since a new voltage is applied. Not to mention, some extra time has to be allocated for the averaging task.

The proposed AI controller is simple but capable of comprehending the system status based on sensor signals and making an optimal choice between the two control inputs. Expectedly, it features robustness with respect to system uncertainties, possessing dual design parameters of ΔV_{ER} and t_d. They are inversely proportional to each other. The larger the former, the smaller the latter can be. More remarkably, depending on the set of their values, the control scheme may experience performance degradation, but the system stability is guaranteed by added positive damping, as is always the case with semiactive controls. The same holds no matter where sensors and actuators are located.

With the controller included, a closed-loop control system is built as in Fig. 5. In the system, the PC computer serves some signal-processing purposes: calculating the whirl radius from gap sensor signals that are shifted by a constant level to retain only pure vibration portions, carrying out the AI control logic, and limiting the maximum voltage of controller output to prevent the breakdown of the ER damper. The shifting of the sensor signals is realized by a circuitry named the level shifter.

5. Computational and experimental results

The mechanical specifications of the test rig are as follows. In units of mm, the inner and the outer radii, and the thickness of the rotating disk between the supportive bearings

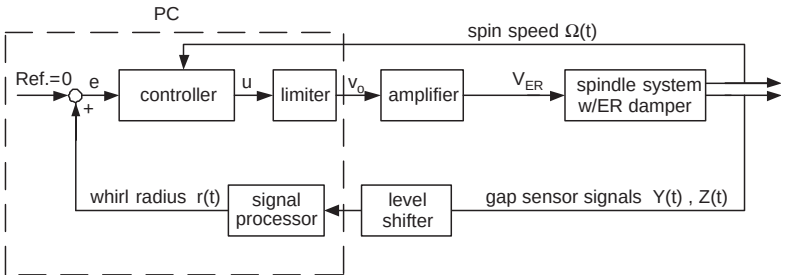

Fig. 5. AI feedback control system.

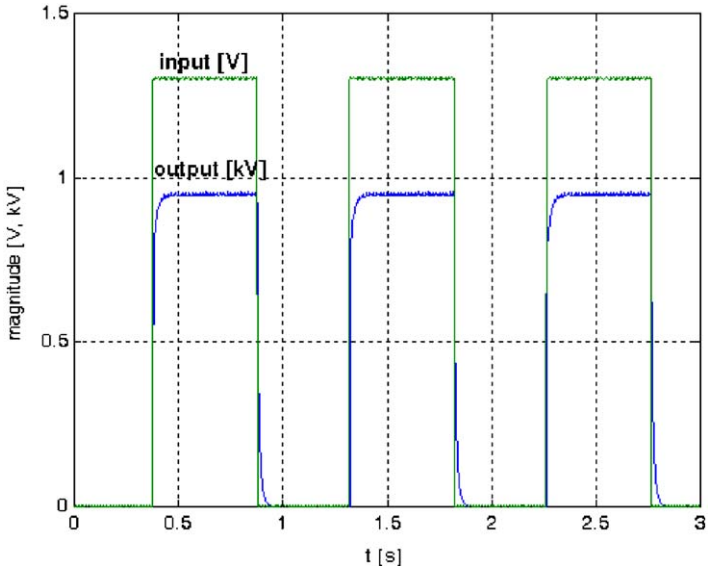

Fig. 6. ER amplifier dynamics.

are, respectively, 6, 100, 1, whereas $L_1 = 350$, $L_2 = 175$, $L_3 = 30$, $L_4 = 60$, $L_5 = 60$, $L_6 = 35.5$, $D_S = 6$, and the clamp thickness = 10; $E_S = E_D = 2.060 \times 10^{11}\,\mathrm{N/m^2}$, $v = 0.3$, $\rho_S = \rho_D = 7800\,\mathrm{kg/m^3}$, $k_B = 3.0 \times 10^7\,\mathrm{N/m}$, and $c_B = 100\,\mathrm{N\,s/m}$. In addition, related to the coupling $\rho_F = 592\,\mathrm{kg/m^3}$, $k_F = 1.31 \times 10^4\,\mathrm{N/m}$, $c_F = 0.2476\,\mathrm{N\,s/m}$, radius = 11 mm, and length = 12.5 mm. Finally, as for the ER fluid and the damper $\alpha = 594.5$, $\beta = 1.517$, $\eta = 0.3227$, $R_o = 45\,\mathrm{mm}$, $R_i = 10\,\mathrm{mm}$, $h = 1\,\mathrm{mm}$, $n = 1$, $m_{\mathrm{ER}} = 48.8\,\mathrm{g}$, and $k_{\mathrm{ER}} = 3266.7\,\mathrm{N/m}$. The fluid in use has cornstarches as the dielectric particles in the non-conducting medium of silicon oil.

From Fig. 6 showing the experimental, dynamic input–output relationship of the voltage amplifier loaded with the damper, it can be found out that τ_A equals 25 ms. Also, the other relevant constants such as $V_{\mathrm{ER\,max}}$ and K_A are determined as 3500 V and 1000, respectively, by checking out the threshold voltage above which the ER damper breaks down and ignoring the

parabolic nonlinearity of voltage gain stretching over the input range from 0 to 5 V, which is observable in Fig. 6.

Throughout all the computations that follow, the rotor system in the present study is to be divided into totally 15 finite elements as displayed in Fig. 7. The reason for such meshes as 2 for the disk and 13 for the shaft lies at the sufficient convergence achieved as in Tables 1 and 2. Note that the damper is located at node 2 on the overhung part to promote control effects, whereas a pair of gap sensors is installed at node 4 just inboard of the left bearing.

Henceforth, in this section, the free response results are to be presented first for system identification purposes, and next the forced response ones such as uncontrolled ER damper effects and AI controlled performances.

5.1. Natural vibration modes

Performing modal analysis based on Eq. (9), individual vibration modes and their natural frequencies can be predicted with the ER voltage set to zero. Shown in Figs. 8 and 9 are the

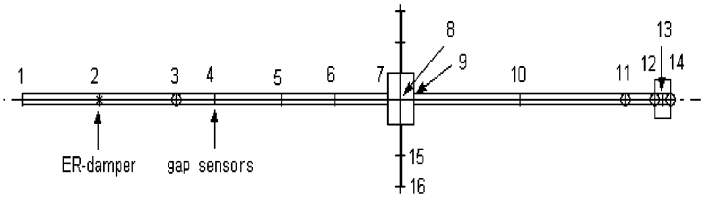

Fig. 7. Finite element meshes.

Table 1
Natural frequencies vs. no. of disk meshes

No. of disk meshes	1st mode (Hz)	2nd mode (Hz)	3rd mode (Hz)
1	46.954	132.399	355.229
2	46.954	132.397	353.194
3	46.954	132.397	352.942

Table 2
Natural frequencies vs. no. of shaft meshes

No. of shaft meshes	1st mode (Hz)	2nd mode (Hz)	3rd mode (Hz)
11	46.955	132.398	354.629
13	46.954	132.397	353.194
15	46.954	132.395	352.966

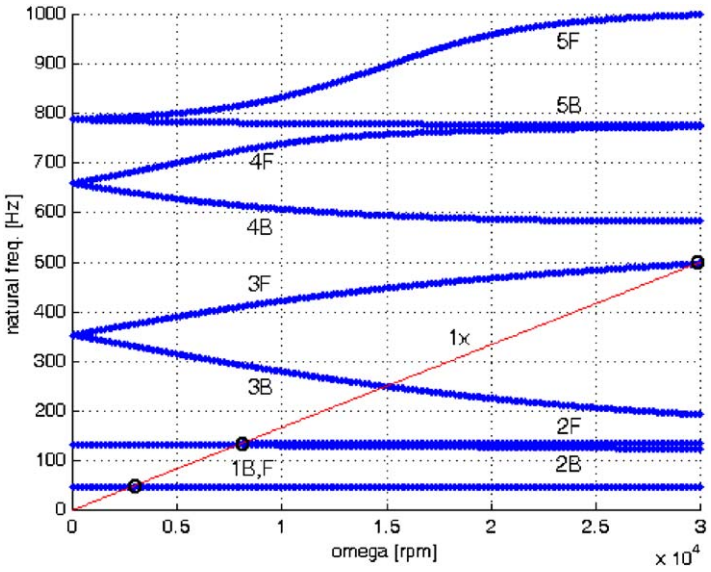

Fig. 8. Campbell diagram.

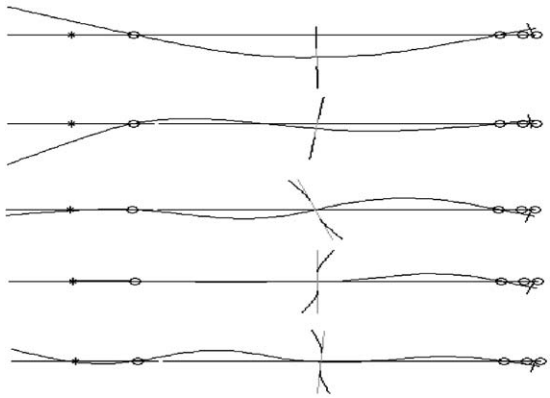

Fig. 9. Lowest mode shapes (from top to bottom).

Campbell diagram and the natural mode shapes associated with the five lowest modes at the stationary state.

Fig. 8 reveals that the first mode does not branch with the spin speed varied, involving little gyro effect in contrast to the other modes. Along with the circle marks, the auxiliary straight line labeled with 1x in the figure graphically indicates where the synchronous critical speeds exist. In addition, the letters, 'B' and 'F' denote the backward and forward whirls of each mode. Remarkably, all the deformed mode shapes of disk in Fig. 9 are of single nodal diameter, coupling with the flexural vibration of the shaft in accordance with the proved principle [9].

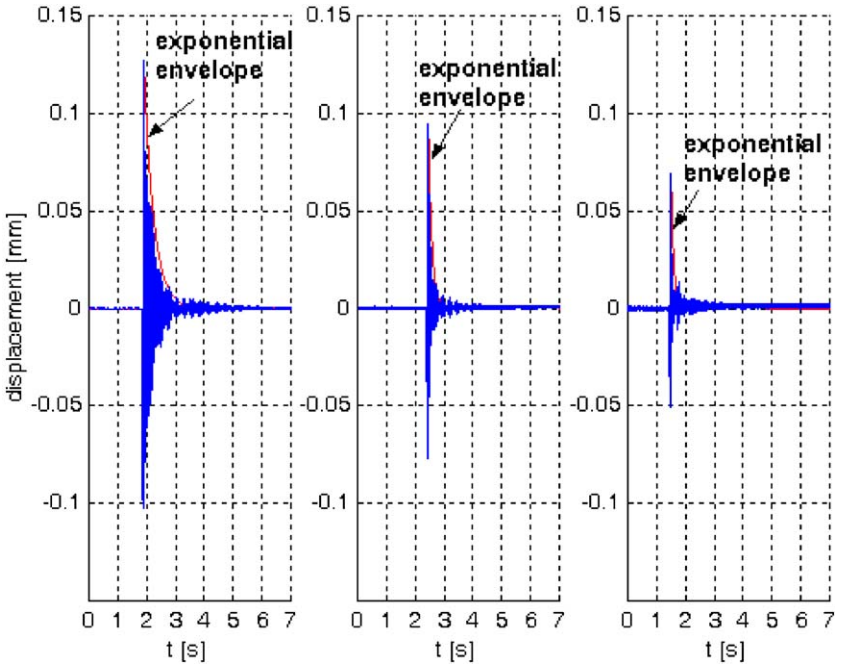

Fig. 10. Impulse responses when $V_{ER} = 0$, 0.5, and 1.5 kV (from left to right).

5.2. Impulse response

In order to experimentally check the dynamic characteristics of the constructed ER damper and the time constant of the overall system, an impact was applied to the rotor system at node 5 while the system is stationary. As a result, the time responses in Fig. 10 were observed, the signal envelopes consistently indicating that the exponentially decaying viscous damping dominates only for the initial period when the shear rate is fairly large, whereas the linearly decaying Coulomb damping overtakes later on as the shear rate grows smaller. This backs up the assumption that the ER fluid behaves according to the Bingham fluid model.

In addition, the leftmost plot of the same figure informs that the system time constant approximately equals 0.3 s in the case of null ER voltage, which can be also confirmed by the computed eigenvalue of the first vibration mode. As the voltage magnitude increases, the larger damping develops to shorten the time constant. For instance, it is seen less than 0.1 s when $V_{ER} = 1.5$ kV.

5.3. Frequency response function

To validate the computed natural frequencies mentioned in the preceding subsection, a frequency response function (FRF) was experimentally obtained as in Fig. 11 at the stationary state, by striking downward the shaft at node 5 with an impulse hammer while

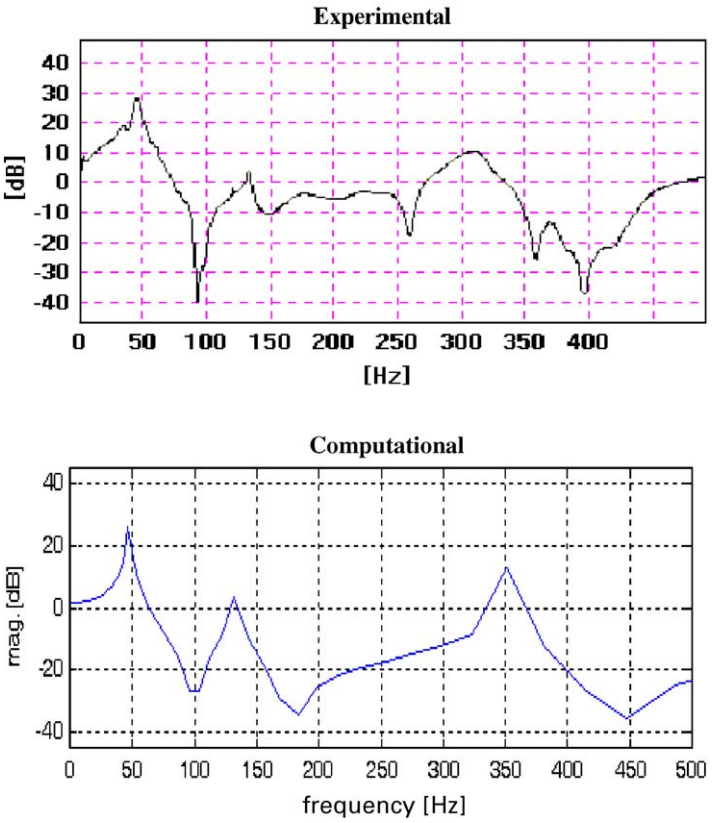

Fig. 11. FRFs at 0 rev/min.

measuring the excited vibration displacements with a gap sensor. It confirms decent agreements for the first two modes at 45 and 130 Hz, whereas for the third the computed value of 353 Hz is about 10% higher than the experimental one, 320 Hz. Such a discrepancy is considered mainly due to the simple, lumped modeling of the flexible coupling that has inherently distributed parameters. Nevertheless, such inaccuracy is immaterial since the third mode is far beyond the experimental speed range.

For the same situation, an FRF was computed as in Fig. 11 from Eq. (9), which assures the preciseness of the mathematical model up to above the second mode. For direct comparisons between the magnitudes in the two subplots of Fig. 11, the vertical-axis scale of lower one is converted to the unit of decibel (dB) and added by 100 dB reflecting the calibrated gains of the employed hammer and sensor.

5.4. *Uncontrolled ER damper effects (at steady state)*

It is of some interest to investigate how the ER damper actually influences rotor vibration in the presence of numerous vibration sources. For present numerical simulations, however, only

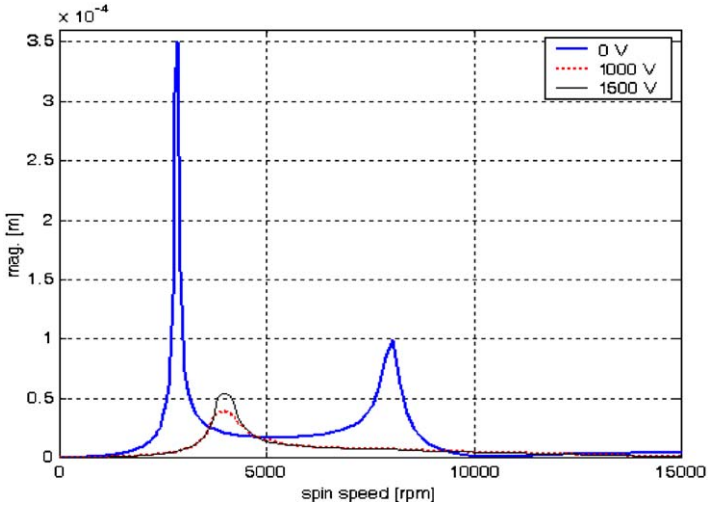

Fig. 12. Computed ER damper effect.

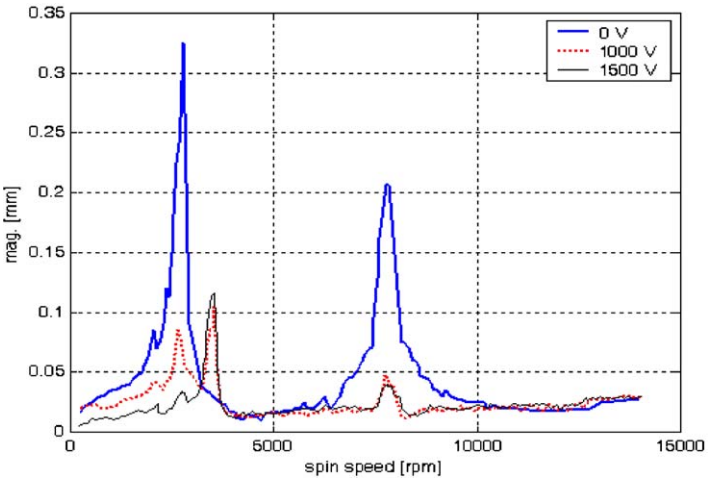

Fig. 13. Experimental ER damper effect.

eccentricity is considered on the ground that it is usually the major exciter. Assuming an unbalance mass of 4 g 2 mm away radially from the rotating disk center, the unbalance response at steady state was computed as in Fig. 12 for three distinct, constant ER damper voltages. Meanwhile, the corresponding experimental results were obtained as in Fig. 13.

On comparisons between the two figures, some magnitude difference is observed. It is attributable to uncertainties of the eccentricity, existence of extra vibration sources, errors in the models of the ER fluid and the amplifier, etc. One more reason to point out is the asymmetry of the experimental whirl orbit that is prominent especially when the whirl becomes large. Whereas

the whole system is assumed axisymmetric in modeling, the actual test rig turns out somewhat different for the reason to be discussed later. This makes the measurement of whirl magnitudes taken along the horizontal Z-axis give rise to larger amplitudes than calculated around all the peaks.

Overall, however, the trends coincide; the ER damper reduces vibration in the range stretching from the rest to a certain speed above the first resonance, but thereafter the converse is true up to another certain speed. As each resonance is traversed, such a phenomenon repeats itself successively and becomes stronger in proportion to the input voltage.

The shift of whirl peaks toward the higher frequency with decreased magnitudes results from the stiffening effect of the so-called point damper acting at a point of a flexible rotor. As the electric field intensifies, the whirl at the damper location shrinks furthermore due to the opposing damping force. In this sense, the damper acts as if it were a supportive bearing constraining motions. Such a bearing-like effect changes not only the mode shapes but also raises the critical speeds. To verify this, a simulation was done treating the ER damper as the third bearing of the same stiffness and damping properties as the others. The outcomes are Figs. 14–16 revealing the

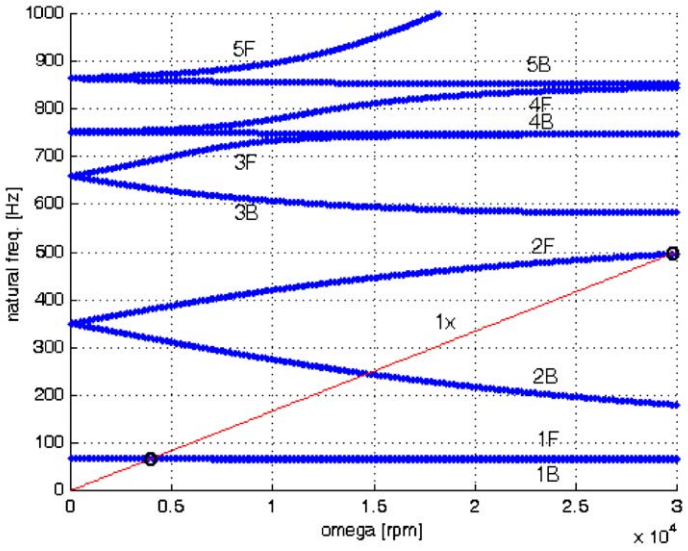

Fig. 14. Campbell diagram when the ER damper is treated as a bearing.

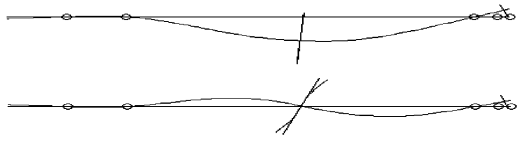

Fig. 15. Lowest mode shapes when the ER damper is treated as a bearing.

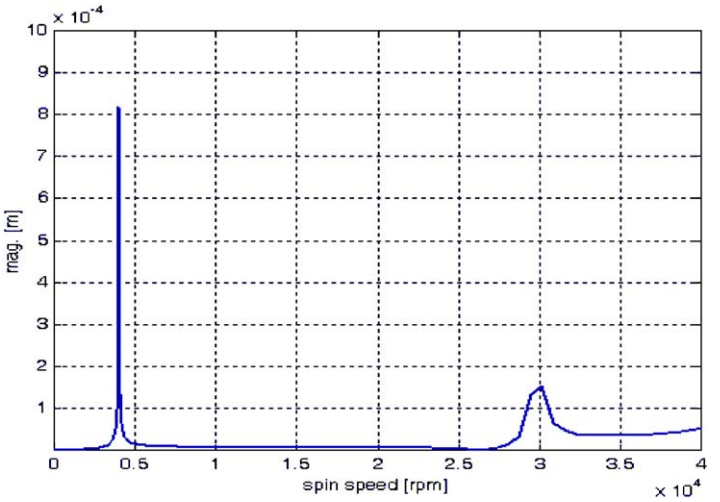

Fig. 16. Unbalance response when the ER damper is treated as a bearing.

natural frequencies and specifically the shapes and the critical speeds associated with the changed first two modes. One appears at 3960 rev/min very close to the shifted peak in Fig. 13 involving a little gyro effect, and the other at 30,000 rev/min out of that figure scope resembling the third mode shape in the case of null V_{ER}. This stiffening effect comprehensively accounts for the rise of the first critical speed reported in Refs. [3,7] as well, both of which had an ER damper installed at a discrete location.

5.5. *AI controlled performances*

As mentioned earlier, the two design parameters of the AI controller, namely ΔV_{ER} and t_d, are inversely proportional to each other. For the choice of their values, it is noteworthy that too small a value of the former may degrade the signal-to-noise ratio, making difficult to accurately assess the whirl change rate, but the opposite may lead the system to undergo adverse effects during the transient time period. Therefore, they were determined such that $\Delta V_{ER} = 1\,\text{kV}$ and $t_d = 0.14\,\text{s}$ in consideration of the above-noted nature and the data in Fig. 10.

Using the parameter values, the proposed AI control was carried out both computationally and experimentally to obtain a series of results in Figs. 17–20. In each case, the control was not applied until the steady state was reached, which took about 2 s in numerical simulations done with zero initial state conditions. Refer to Figs. 17–19. The results are presented in the manner comparisons are possible between the initial uncontrolled response of duration t_d and the controlled response after another time lapse as long as $2t_d$, which was needed for the transient response to die out and also for the change rate of averaged whirls to be evaluated. The time history of control input u is also disclosed in each case except for Fig. 20, because the one in question is identical to the input signal in Fig. 17. The spin rates were typically chosen 2.4, 4.5, and 7.5 krev/min from the sub- and

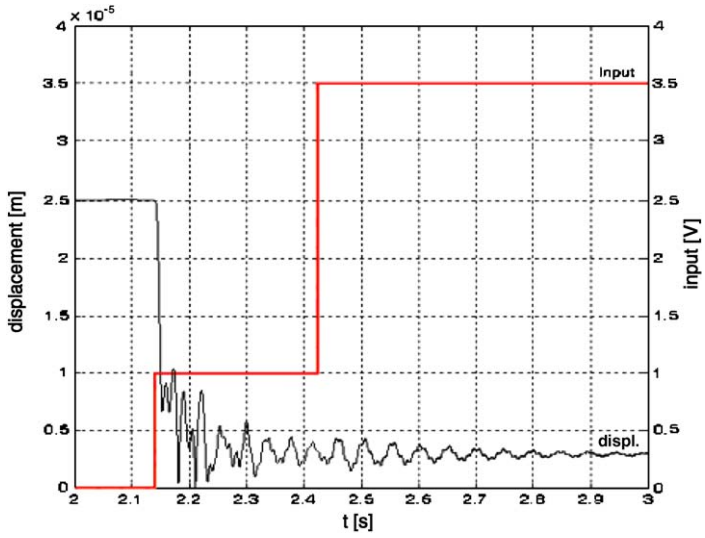

Fig. 17. Computed control response at 2.4 krev/min.

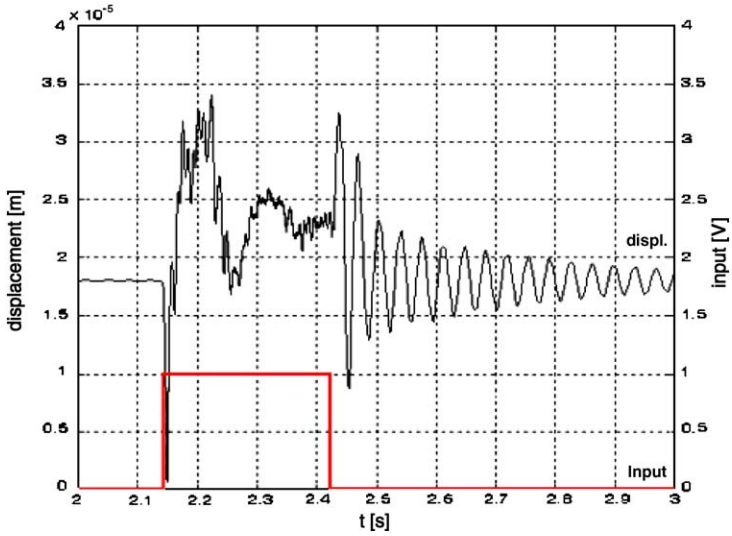

Fig. 18. Computed control response at 4.5 krev/min.

the super-critical speed ranges, and the sampling period for real time control was set to 0.14 ms in common.

The simulation results convince that the ER damper under the AI control can suppress the vibration significantly without producing any negative effects. Moreover, comparisons between Figs. 17 and 20 prove that there exists a strong consistency in trends, and the AI controller

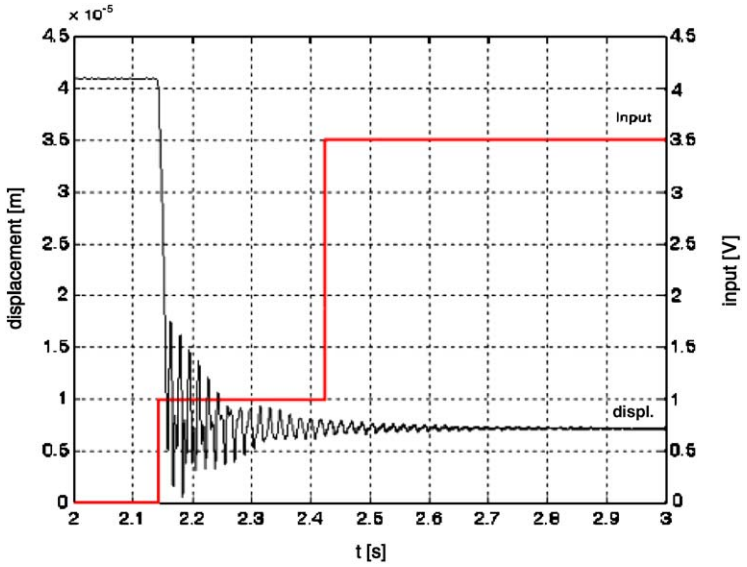

Fig. 19. Computed control response at 7.5 krev/min.

functions robustly despite some magnitude discrepancies. Those quantitative inaccuracies stem from uncertainty of vibration sources, ignorance of temperature-dependent properties of the ER fluid and nonlinearity of the voltage amplifier in the present model, and more critically asymmetry of the system.

The high-frequency contents mingled in the whirl radius signal in Fig. 20 have much to do with the whirl orbit taking an elliptical shape, with its major axis almost horizontal as seen separately in the figure. Such an asymmetry outstands in particular when the orbit grows relatively large, because then occurs a mechanical interference between the mating teeth inside the gear train lacking sufficient clearance along the vertical direction.

Before closing this subsection, it appears worthwhile to check how the PID control performs for the present system. Hence a P control, $u = k_P r$, with the feedback gain of $k_P = 10^5$ V/m was simulated. As expected, it showed as good performances as the AI control at 2.4 and 7.5 krev/min, but not at 4.5 krev/min within the first supercritical range undesirably enlarging the whirl magnitude prior to control. Refer to Fig. 21. This again justifies the use of the proposed AI control.

6. Conclusions

In this paper to suppress flexural vibrations of high-speed rotor systems, a compact damper incorporating the ER fluid was newly designed, and the mathematical models for it and its associated voltage amplifier were derived. Subsequently, they were assembled with finite element models of the other relevant spindle components to obtain the equations of motion for the entire rotor system. Based on the resulting model, a semiactive AI feedback controller was

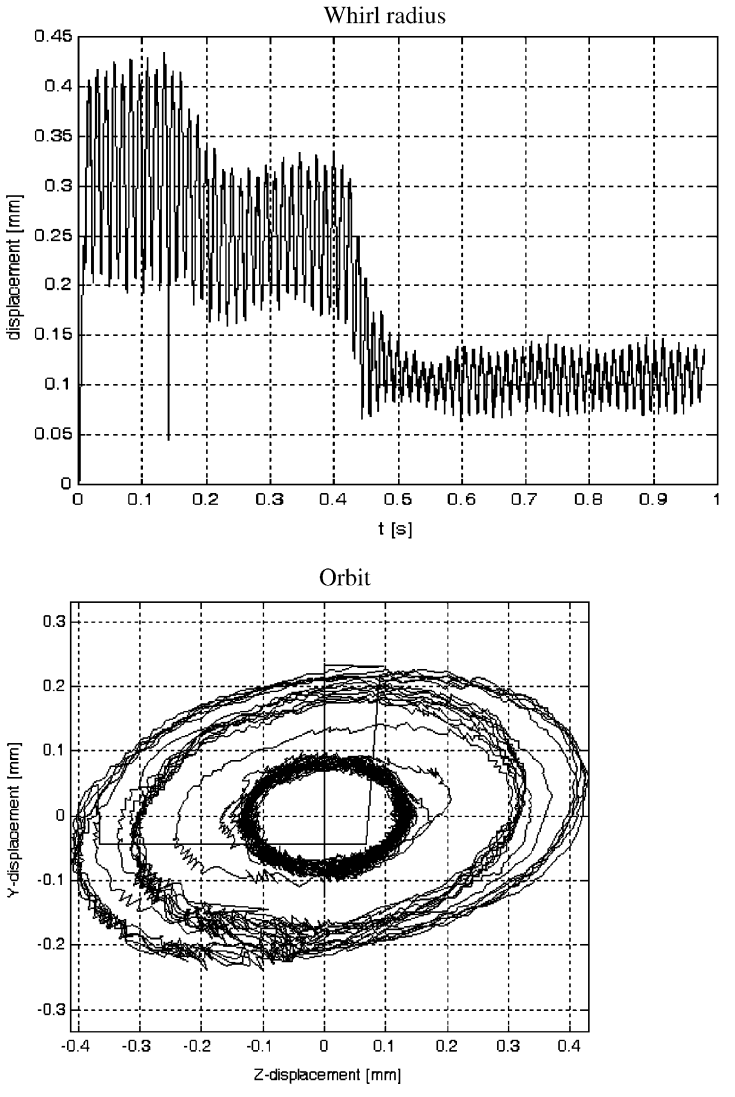

Fig. 20. Experimental control response at 2.4 krev/min.

synthesized, taking into account the stiffening effect of the point damper in flexible rotor applications.

To validate the model, a series of experiments were performed in parallel with numerical simulations. Consequently, the fidelity of the model was proved up to experimental speed range by free responses. On the other hand, as far as the forced responses are concerned, there remain some magnitude disagreements primarily due to uncertainty of vibration sources, simplification of the ER fluid and the amplifier dynamics, and the system asymmetry. However, the computed and experimental results well coincide in trends.

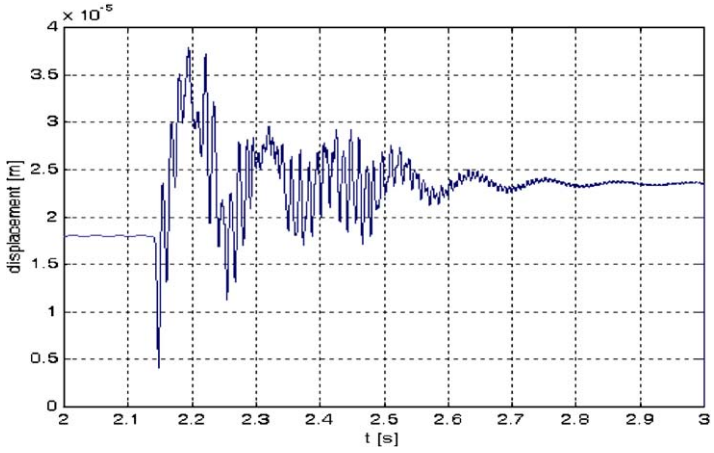

Fig. 21. Computed P control response at 4.5 krev/min (whirl radius).

Finally, as predicted by the simulations the AI controller showed excellent robustness and control performances without any negative effects in practice, regardless of the modeling errors and the operating spin speeds of the system.

References

[1] D. Lubell, L. San Andres, Imbalance response of a test rotor supported on squeeze film dampers, *Journal of Engineering for Gas Turbines and Power* 120 (1998) 397–404.
[2] M.E.F. Kasarda, P.E. Allaire, R.R. Humphris, L.E. Barrett, A magnetic damper for first-mode vibration reduction in multimass flexible rotors, *Journal of Engineering for Gas Turbines and Power* 112 (1990) 463–469.
[3] G.Z. Yao, Y. Qiu, G. Meng, T. Fang, Y.B. Fa, Vibration control of a rotor system by disk type electrorheological damper, *Journal of Sound and Vibration* 219 (1999) 175–188.
[4] S.B. Choi, W.Y. Choi, Position control of a cylinder using a hydraulic bridge circuit with ER valves, *Journal of Dynamic Systems, Measurement, and Control* 122 (2000) 202–209.
[5] K. Nakamura, M. Maruyama, S. Ueha, A new ultrasonic motor using electro-rheological fluid and torsional vibration, *Ultrasonics* 34 (1996) 261–264.
[6] F. Gordaninejad, A. Ray, H. Wang, Control of forced vibration using multi-electrode electro-rheological fluid dampers, *Journal of Vibration and Acoustics* 119 (1997) 527–531.
[7] J.M. Vance, D. Ying, Experimental measurements of actively controlled bearing damping with an electrorheological fluid, *Journal of Engineering for Gas Turbines and Power* 122 (2000) 337–344.
[8] P.G. Nikolakopoulos, C.A. Papadopoulos, Controllable high speed journal bearings, lubricated with electro-rheological fluids. An analytical and experimental approach, *Tribology International* 31 (1998) 225–234.
[9] S. Lim, Finite element analysis of flexural vibrations in hard disk drive spindle systems, *Journal of Sound and Vibration* 234 (2000) 601–616.
[10] S.J. Russel, P. Norvig, *Artificial Intelligence: A Modern Approach*, Prentice Hall, Englewood Cliffs, NJ, 1994.
[11] J.M. Ginder, S.L. Ceccio, The effect of electrical transients on the shear stresses in electrorheological fluids, *Journal of Rheology* 39 (1995) 211–234.
[12] A.D. Dimarogonas, S. Haddad, *Vibration for Engineers*, Prentice Hall, Englewood Cliffs, NJ, 1992.
[13] G. Genta, *Vibration of Structures and Mechanics*, Springer, Berlin, 1988.
[14] W.L. Brogan, *Modern Control Theory*, Prentice Hall, Englewood Cliffs, NJ, 1991.